genotype were obtained by cell sorting and stimulated for 8 hours with Con A (5 μg/ml) before preparation of a cytospin. Cytologic studies were performed on cytocentrifuged smears, which were air-dried, fixed in cold acetone, rehydrated in phosphate-buffered saline, and then stained with monoclonal antibody (mAb) to IL-2 (JES6-1A12) by means of an immunoperoxidase technique (*23*). IL-2$^{-/-}$ mutant mice demonstrate normal thymocyte subsets, confirming that IL-2 is not required for normal T cell ontogeny (*24*). Our observations in young and older heterozygous mice that only 50% of the mature CD4$^+$ and CD8$^-$ thymocytes stained for IL-2 further emphasizes the lack of a developmental advantage for thymocytes that produce IL-2.

8. In 96-well, round-bottom plates, 5 × 10^4 irradiated (2000 centigrays) splenic feeder cells from IL-2$^{-/-}$ mice were cultured at a final volume of 25 μl in complete RPMI 1640 medium containing Con A (5 μg/ml). Each well was subsequently seeded by flow cytometry with various numbers of CD4$^+$ peripheral T cells and grown for 30 hours at 37°C. After freezing and thawing of the plates, 50 CTLL-20 cells and mAb to IL-4 were added to each well in a final volume of 25 μl, and plates were cultured for an additional 28 hours. Live CTLL-20 cells were then rescued by exogenous IL-2 (10 U/ml) added every other day. Seven days after the addition of indicator cells, wells were scored for CTLL-20 cell growth either by examination under the microscope or by ^{3}H-labeled thymidine incorporation. Wells not seeded initially by CD4$^+$ T cells but treated identically as outlined above served as negative controls, whereas the simultaneous addition of IL-2 and CTLL-20 cells served as the positive control. This measurement of IL-2 corresponds to a modified method of (*25*).
9. G. A. Holländer, K. Mobisson, S. J. Burakoff, unpublished results.
10. S. Kramer *et al.*, *Eur. J. Immunol.* **24**, 2317 (1994).
11. H. Sakamoto *et al.*, *Proc. Natl. Acad. Sci. U.S.A.* **88**, 10890 (1991).
12. Fixed and rehydrated cytocentrifuged smears were stained with biotinylated mAb to IL-2 (JES6-5H4) followed by avidin-coupled fluorescein isothiocyanate (FITC) (Becton Dickinson). Single cells were scanned by ACAS interactive laser cytometry, and ACAS software (Meridian Instruments) was used to analyze the fluorescence scans.
13. F. Matesanz and A. Alcina, *Eur. J. Immunol.* **26**, 1675 (1996); _____ and A. Pellicer, *Immunogenetics* **38**, 300 (1993).
14. T cells from C57BL/6, *M. spretus*, and (C57BL/6 × *M. spretus*) F$_1$ were stimulated in bulk by phorbol 12-myristate 13-acetate and calcium ionophore A23187 for 10 hours. CD4$^+$ T cells were then sorted by flow cytometry as single cells into 10 μl of 2× reverse transcription (RT) buffer containing 0.05% NP-40 and immediately frozen on dry ice. RT was done on single-cell lysates or fractions thereof with an IL-2–specific primer (GTGTTGTAAGCAGGAGGTACATAGTTA) followed by 30 cycles of a first PCR amplification (5′: CATGCAGCTCGCATCCTGTGT; 3′: GTGTTGTAAGCAGGAGGTACATAGTTA). One microliter of a 50-μl reaction was used for a seminested second amplification of 26 cycles (5′: GAGCAGGATGGAGA ATTACAGG; 3′: GTGTTGTAAGCAGGAGGTACATAGTTA). The amplicons differ by a Fnu 4HI–sensitive sequence that allows the distinction of maternal C57BL/6 from paternal *M. spretus* DNA. The PCR reaction was analyzed on a 2% agarose gel after digestion of the amplicons. The expected product from the paternal *M. spretus* allele is 358 base pairs (bp), whereas the larger fragment of the digested C57BL/6 maternal allele is 229 bp (the smaller fragment of 129 bp is not shown in Fig. 4A). The single-cell RT-PCR used would be sufficiently sensitive to detect biallelic transcription if it were present because IL-2–specific transcripts can still be amplified from 1:4 dilution of single-cell lysates. Moreover, mixing RNA at diverse ratios followed by RT-PCR allowed for the concurrent detection of both transcripts over a broad range of different concentrations (*26*).
15. G. P. Holmquist, *Am. J. Hum. Genet.* **40**, 151 (1987).
16. J. H. Taylor, *J. Biophys. Biochem. Cytol.* **7**, 455 (1960); D. Kitsberg *et al.*, *Nature* **364**, 459 (1993); J. H. Knoll, S. D. Cheng, M. Lalande, *Nature Genet.* **6**, 41 (1994).
17. J. B. Lawrence, C. A. Villanave, R. A. Singer, *Cell* **52**, 51 (1988). A modified protocol was developed for FISH. Mitogen-stimulated T cells enriched for S phase by flow cytometry were harvested, incubated (0.075 M KCl, 37°C for 15 min), fixed (3:1, methanol: acetic acid), dropped onto clear slides, and then air-dried overnight. Before hybridization, slides were treated with ribonuclease A for 1 hour at 37°C, digested with pepsin in 10 mM HCl for 3 min at 37°C, and postfixated in 1% acid-free formaldehyde, 1× PBS, and 50 mM $MgCl_2$ (pH 7.0) for 10 min at room temperature. The probes used, c-*mpl* and *IL-2*, were labeled by random priming with biotinylated 14-deoxycytidine triphosphate (Gibco-BRL). Cytogenetic preparations were denatured, immediately dehydrated, and then air-dried before overnight hybridization with denatured probes. The slides were then rinsed, and the signal was detected and amplified by incubation with FITC-conjugated avidin and biotinylated goat antibody to avidin (2 μg/ml each; Vector Laboratories). Samples were stained with propidium iodine for 5 min at 0.1 μg/ml in PBS and mounted. Samples were visualized at 100× magnification on a Zeiss microscope (Axiophot) equipped with epifluorescence optics for 4′,6′-diamidino-2-phenylindole and fluorescein. Images taken were intensified with the Nu200 charge-coupled device Camera System (Photometrics) and then processed with IPLabSpectrum (Signal Analytics) software.
18. K. Pfeifer and S. M. Tilghman, *Genes Dev.* **8**, 1867 (1994).
19. A. Chess, I. Simon, H. Cedar, R. Axel, *Cell* **78**, 823 (1994).
20. D. G. Schatz, M. A. Oettinger, M. S. Schlissel, *Annu. Rev. Immunol.* **10**, 359 (1992); M. M. Davis, *Cell* **59**, 475 (1990).
21. L. Fiorentino, D. Austen, D. Pravtcheva, F. H. Ruddle, E. Brownell, *Genomics* **5**, 651 (1989); G. C. Webb, H. D. Campbell, J. S. Lee, I. G. Young, *Cytogenet. Cell Genet.* **54**, 164 (1990); C. V. Beechey and B. M. Cattanach, *Mouse Genome* **92**, 108 (1994).
22. N. J. Holbrook *et al.*, *Proc. Natl. Acad. Sci. U.S.A.* **81**, 1634 (1984); A. Fuse *et al.*, *Nucleic Acids Res.* **12**, 9323 (1984).
23. N. Cerf-Bensussan, A. Quaroni, J. T. Kurnick, A. K. Bhan, *J. Immunol.* **132**, 2244 (1984); P. Mombaerts *et al.*, *Cell* **75**, 275 (1993); S. A. Bogen, I. Fogelman, A. K. Abbas, *J. Immunol.* **150**, 4197 (1993).
24. H. Schorle, T. Holtschke, T. Hunig, A. Schimpl, I. Horak, *Nature* **352**, 621 (1991).
25. B. Rocha and A. Bandeira, *Scand. J. Immunol.* **27**, 47 (1988).
26. G. A. Holländer *et al.*, data not shown.
27. We thank I. Horak for the IL-2 knockout mice and the genomic IL-2 clone; R. Skoda for the c-*mpl* clone; A. Surani for the (C57BL6/6 × *M. spretus*) mice; P. Yacono and E. Ten Boekel for excellent technical assistance; and G. Balciunaite, J. Bluestone, W. Gehring, J. Seidman, C. Steinberg, and R. Zeller for helpful discussions. Supported by a grant from the Swiss National Science Foundation (31-43'600.95 to G.A.H.) and grants from the NIH (PO1 CA39542-09 and RO1 AI17258-18 to S.J.B, RO1 DK47677 to A.K.B., P30 DK43351 to A.K.B and C.T., and HL32854 and HL15157 to D.E.G.).

3 April 1997; accepted 19 February 1998

Structure of Nitric Oxide Synthase Oxygenase Dimer with Pterin and Substrate

Brian R. Crane,* Andrew S. Arvai, Dipak K. Ghosh, Chaoqun Wu, Elizabeth D. Getzoff, Dennis J. Stuehr,† John A. Tainer†

Crystal structures of the murine cytokine-inducible nitric oxide synthase oxygenase dimer with active-center water molecules, the substrate L-arginine (L-Arg), or product analog thiocitrulline reveal how dimerization, cofactor tetrahydrobiopterin, and L-Arg binding complete the catalytic center for synthesis of the essential biological signal and cytotoxin nitric oxide. Pterin binding refolds the central interface region, recruits new structural elements, creates a 30 angstrom deep active-center channel, and causes a 35° helical tilt to expose a heme edge and the adjacent residue tryptophan-366 for likely reductase domain interactions and caveolin inhibition. Heme propionate interactions with pterin and L-Arg suggest that pterin has electronic influences on heme-bound oxygen. L-Arginine binds to glutamic acid–371 and stacks with heme in an otherwise hydrophobic pocket to aid activation of heme-bound oxygen by direct proton donation and thereby differentiate the two chemical steps of nitric oxide synthesis.

Nitric oxide synthases (NOSs) oxidize L-Arg to synthesize nitric oxide (NO), which is a key intercellular signal and defensive cytotoxin in the nervous, muscular, cardiovascular, and immune systems (*1*, *2*). Neuronal NOS (nNOS, NOS1) and endothelial NOS (eNOS, NOS3) produce low NO concentrations for neurotransmission, insulin release, penile erection, vasorelaxation, oxygen detection, and memory storage, whereas cytokine-inducible NOS (iNOS, NOS2) produces larger NO concentrations to counter pathogens and coordinate the T cell response (*1*). NOSs catalyze two sequential, mechanistically distinct, heme-based oxidations in the five-electron oxidation of L-Arg to L-citrulline (L-Cit) and

B. R. Crane, A. S. Arvai, E. D. Getzoff, J. A. Tainer, Department of Molecular Biology and Skaggs Institute for Chemical Biology, The Scripps Research Institute, La Jolla, CA 92037, USA.
D. K. Ghosh, C. Wu, D. J. Stuehr, Department of Immunology, The Lerner Research Institute, Cleveland Clinic, Cleveland, OH 44195, USA.

*Present address: Beckman Institute, California Institute of Technology, Pasadena, CA 91125, USA.
†To whom correspondence should be addressed.

NO. First, L-Arg is hydroxylated to N^{ω}-hydroxy-L-arginine (NOH–L-Arg) by a mixed-function oxidation (*2*) analogous to reactions catalyzed by the cytochrome P-450s with a proposed oxo-iron intermediate [P$^{\cdot}$-Fe(IV)=O, where P$^{\cdot}$ is a porphyrin π-cation radical] (*3*). Second, NOH–L-Arg is converted to L-Cit and NO by an unusual mechanism involving a one-electron oxidation of NOH–L-Arg and a proposed peroxo-iron intermediate [P-Fe(III)-OO^{2-}] (*2*).

Each NOS isozyme contains a catalytic NH_2-terminal oxygenase domain (NOS_{ox}, residues 1 to 498 for iNOS) and a COOH-terminal electron-supplying reductase domain (NOS_{red}, residues 531 to 1144 for iNOS) (*2*). NOS_{ox} binds heme (iron protoporphyrin IX), tetrahydrobiopterin [(6*R*,1′*R*,2′*S*)-5,6,7,8 tetrahydrobiopterin or H_4B], and substrate L-Arg. NOS_{red} is homologous to cytochrome P-450 reductase and binds flavin mononucleotide, flavin adenine dinucleotide, and the reduced form of nicotinamide adenine dinucleotide phosphate. An intervening calmodulin-binding region (residues 499 to 530 for iNOS) regulates reduction of NOS_{ox} by NOS_{red}. In all three isozymes, H_4B binding and NOS_{ox} dimerization are essential for catalytic activity (*2*). Recently, structures of monomeric murine $iNOS_{ox}$ Δ114 (residues 115 to 498) revealed the unusual topology and heme environment of NOS_{ox} (*4*) but lacked H_4B and NH_2-terminal residues 77 to 114, components required for activity.

Here we report three structures of fully functional, pterin-loaded, dimeric murine macrophage $iNOS_{ox}$ [residues 66 to 498 (*5*)]: with substrate L-Arg (H_4B-ARG, 2.6 Å resolution), with product analog thiocitrulline (SCit) (H_4B-SCIT, 2.7 Å resolution), and without bound ligands (H_4B-H_2O, 2.6 Å resolution) (*6*–*8*). In the symmetric $iNOS_{ox}$ dimer (90 by 70 by 45 Å^3, Fig. 1), mobile and exposed hydrophobic regions identified in the $iNOS_{ox}$ Δ114 monomer (*4*) refold to buttress the substrate-binding channel and sequester two molecules of H_4B within two symmetry-related helical lariats (Figs. 1 and 2A) at the heart of the extensive dimer interface (2800 Å^2 of buried surface area from more than 85 residues per subunit, Fig. 2B). Except for these drastic changes at the interface (Fig. 2C), each subunit maintains the monomer's unusual winged β-sheet fold that resembles a left-handed baseball catcher's mitt (*4*) (Fig. 1). The two helical lariats (Figs. 1 and 2A), each composed of two 3_{10} helices, α10 (residues 454 to 459) and α11 (residues 463 to 471, kinked at residue 467 into α11a and α11b), associate around the two pterins, each of which bridges (Fig. 3A) the COOH-terminal ends of α10 and α11a* (stars indicate the symmetry-related subunit). Helical T's, named for the T shape formed from α8 and α9 (Fig. 2), self-associate symmetrically to frame the helical lariats and bound pterins (Figs. 1B, 2A, and 2B). The NH_2-terminal residues not present in $iNOS_{ox}$ Δ114 (primed nomenclature) form an NH_2-terminal hook (composed of antiparallel strands β1′ and β2′, residues 77 to 100) that reaches across to the other subunit to interact with β12* and the COOH-terminal end of α9* (Figs. 1 and 2) and thereby influence iNOS dimer formation and activity (*5*, *9*). An irregular extended strand comprising residues 108 to 114 (the NH_2-terminal pterin-binding segment) makes important contacts with the pterin (Figs. 2 and 3) and is bridged to the NH_2-terminal hook by Glu^{473*}. In the crystal, Cys^{109}, the only isozyme-conserved cysteine to affect dimer formation and H_4B binding in iNOS and nNOS (*5*, *10*), forms a symmetric disulfide bond across the dimer interface (Fig. 1A). The preceding, disordered, isozyme-variable surface loop (residues 101 to 107) is near its own symmetry mate (Fig. 1B), suggesting that the NH_2-terminal hooks may swap from intersubunit to intrasubunit interactions during dimer-to-monomer transitions.

Dimerization creates a ~30 Å deep, funnel-shaped active-center channel from the shallow ~10 Å distal heme pocket present in the monomeric $iNOS_{ox}$ Δ114 structure (*4*) by refolding and recruiting components of the dimer interface: α7a, the pterin, the NH_2-terminal pterin-binding segment, and the NH_2-terminal hook (Figs. 1 and 2). Helix α7a (residues 370 to 378, Fig. 2A) supplies residues that interact with both substrate and pterin (Figs. 3 and 4). The channel, which is formed primarily by the residues of one subunit, narrows from an ellipsoid mouth ~9 by 15 Å^2 bracketed by Trp^{84}, Ala^{276}, Gln^{381}, and Glu^{488} to the

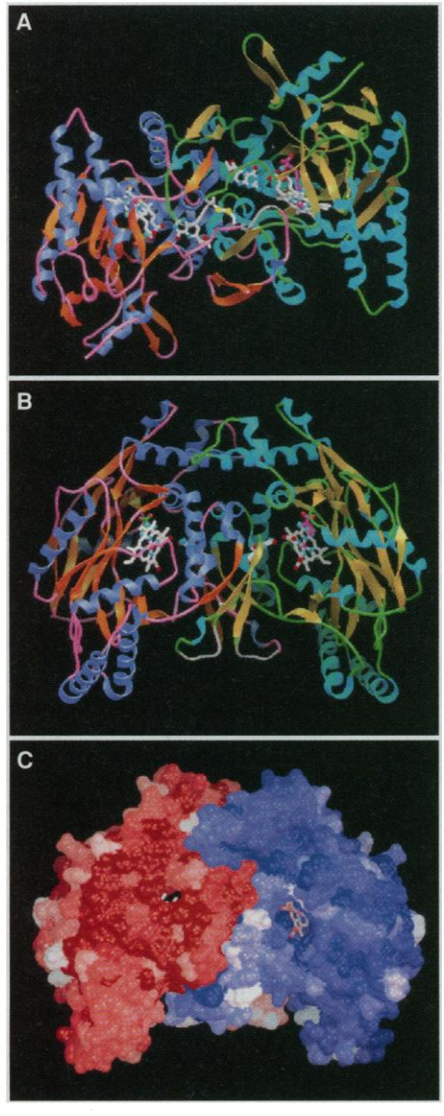

Fig. 1. NOS_{ox} α-β fold, dimer assembly, and likely interaction surface for NOS_{red} and caveolin. (**A**) The symmetric $iNOS_{ox}$ dimer viewed along the crystallographic twofold axis, showing left (and right) subunits with orange (yellow) winged β sheets and flanking blue (cyan) helices. Ball-and-stick models (white bonds with red oxygen, blue nitrogen, yellow sulfur, and purple iron atoms) highlight active-center hemes (left-most and right-most), interchain disulfide bonds (center, foreground), pterin cofactors (white, left-center and right-center), and substrate L-Arg (green left and magenta right). The NH_2-terminal ends contribute β hairpins (center top and bottom) to the dimer interface, and the COOH-termini (lower left and upper right) lie 85 Å apart. Gray loops (residues 101 to 107) are disordered. (**B**) $iNOS_{ox}$ dimer shown rotated 90° about a horizontal axis from (A). Each heme is cupped between the inward-facing palm (webbed β sheet) and thumb (magenta loop in front of left heme and green loop behind right heme) of the "catcher's mitt" subunit fold. (**C**) Solvent-accessible surface (*29*) of the $iNOS_{ox}$ dimer (one subunit red, one subunit blue) oriented as in (B) and color-coded by residue conservation (paler to more saturated represents less conserved to more conserved) in NOS_{ox} sequences of known species and isozymes. The heme (white tubes) is also solvent-exposed on the side (left subunit) opposite the active-center channel (right subunit) and surrounded by a highly conserved hydrophobic surface for NOS_{red} and caveolin binding. (Stereo variations of Figs. 1 through 4 are available at www.scripps.edu/~jat.)

L-Arg guanidinium-binding site above the heme's distal face (Figs. 1C and 3B). The zigzag β-strand transitions (*4*) that structure the winged β sheet may be important for funneling dioxygen to the heme iron as they form the side of the active-center channel that remains open when L-Arg is bound (Figs. 1C and 4A).

Conformational changes on dimerization expose the heme edge on the side opposite to the active-center channel and provide a likely interaction surface (Fig. 1C) for complementarily shaped NOS_{red}, on the basis of P-450 reductase homology (*11*). The α9 helix pivots 35° (Fig. 2C) to uncover a hydrophobic pocket, conserved across species and isozymes, that includes Trp^{366} and the heme pyrrole ring C methyl and vinyl groups (Figs. 1C and 4). In fact, caveolin-1 and -3, which target eNOS to the plasma membrane caveolae and inhibit NO synthesis in a manner reversed by calmodulin (*12*), bind conserved NOS residues that are included in the surface implicated above for NOS_{red} interactions. Thus, caveolin binding may biologically regulate NOS by blocking NOS_{red} from supplying electrons to the heme via pyrrole ring C (Fig. 3B).

The $iNOS_{ox}$ dimer structure supports a fundamental role for pterin H_4B in controlling iNOS subunit interactions (*13*) and active-center formation, but not for pterin directly hydroxylating L-Arg or activating heme-bound oxygen (Fig. 3). H_4B stabilizes the dimer by integration into the hydrophobic heart of the interface and facilitates substrate interactions by lining the active-center channel and hydrogen bonding to a heme propionate and to α7, two elements involved in L-Arg binding (Fig. 3). In the NOS dimer, H_4B sits proximal and perpendicular to the heme, with its 2-amino-4-hydroxy-pyrimidine ring interacting with the extended propionate from heme pyrrole ring A, its O4- and N5-containing edge presented to solvent in the active-center channel, and its dihydroxy-propyl side chain directed toward the NH_2-terminal hook and second subunit (Figs. 1A, 2, and 3). The helical lariats from both subunits sandwich each pterin with aromatic π-stacking interactions, and the NH_2-terminal pterin-binding segments provide additional contacts and hydrogen bonds to further stabilize the cofactor sites (Fig. 3).

The pterin is positioned for indirect structural and electronic influences on substrate and inhibitor binding and catalysis (*14–17*). Hydrogen bonds bridge from pterin N3 (directly) and O4 (through a water molecule) through heme propionate A to the L-Arg α-amino group, and from pterin O4 (directly) and N5 (through a water molecule) to Arg^{375} of the substrate-binding helix, which participates in an extensive hydrogen-bond network (Fig. 3). In the pterin-free monomer structure (*4*), heme propionate A interacts with Arg^{193} and the α7a helix, where it could block

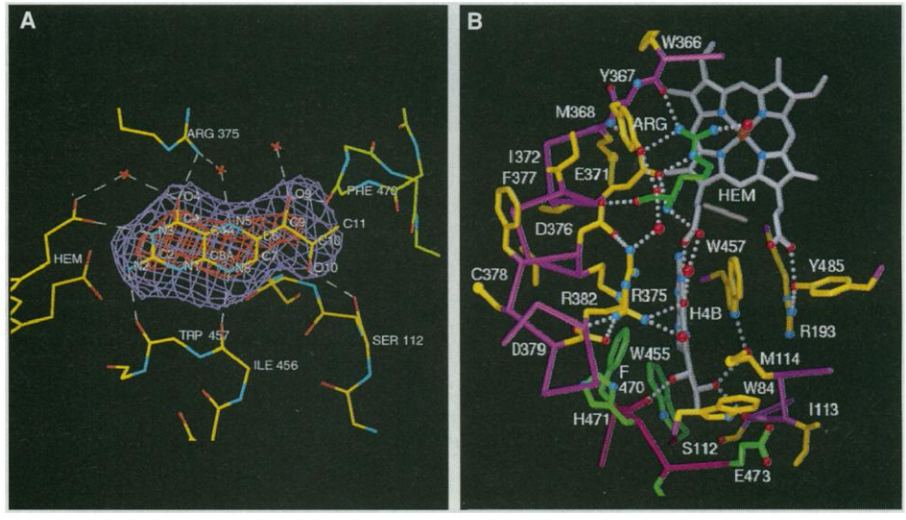

Fig. 3. Pterin interactions in the substrate-binding channel. (**A**) A σ_A-weighted $F_{obs} - F_{calc}$ omit map (purple 3.5σ and red 9.5σ contours) showing well-ordered H_4B (yellow carbon, red oxygen, and blue nitrogen bonds) and its hydrogen bonds (white dashed lines) to each subunit of the dimer (yellow carbons or green carbons). (**B**) The hydrogen-bond network coupling pterin binding, dimerization, L-Arg binding, and heme activity. Heme (HEM, top right) and L-Arg (ARG, green, top center) are bound by one subunit (magenta Cα trace and yellow side chains, with blue nitrogen and red oxygen balls), whereas H_4B (H4B, center edge on) interacts with the helical lariat of the symmetry-related subunit as well (red Cα trace and green side chains, bottom).

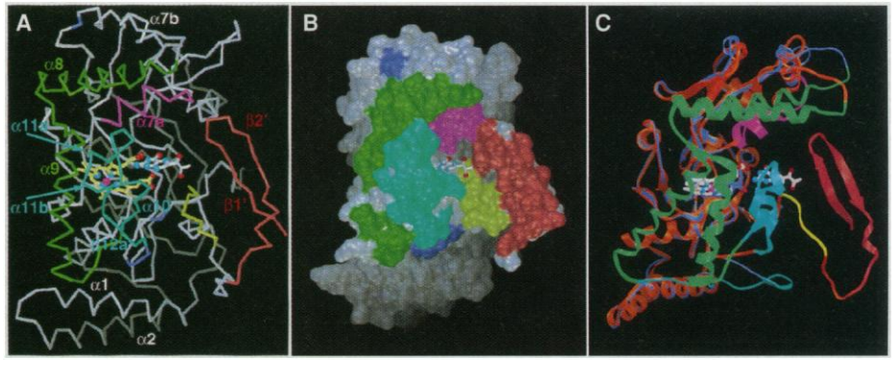

Fig. 2. Dimer interface structural elements and conformational changes on $iNOS_{ox}$ dimerization. (**A**) Cα trace of one $iNOS_{ox}$ subunit viewed directly into the dimer interface. Protein components contributing residues to the extensive dimer interface are separated into six colored regions: NH_2-terminal hook (β1′ and β2′, rose), NH_2-terminal pterin-binding segment (yellow), substrate-binding helix α7a (magenta), helical T (α8 and α9, green), helical lariat (α10, α11a and 11b, and β12a, cyan), and other residues (pale purple). Pterin (white bonds with blue nitrogens and red oxygens, center) interacts with heme (yellow bonds with blue nitrogens and red oxygens, center left). (**B**) The buried surface of the dimer interface color-coded by residues contributed from the regions categorized and colored in (A). (**C**) Superposition of the $iNOS_{ox}$ Δ114 monomer (thin ribbons) onto one subunit of the $iNOS_{ox}$ Δ65 dimer (wide ribbons). Although the core of the winged β-sheet domain is structurally conserved between the monomer (purple) and the dimer (orange) with a Cα rmsd of 0.8 Å for residues 115 to 336 and 480 to 496, large differences do occur at the dimer interface (foreground), with some residues moving up to 40 Å. Dimerization causes formation of the helical lariat (cyan) from a loop and β strand of the monomer (bottom center, blue and purple), reorganization of the substrate-binding helix (α7a, magenta) and following sequence (background, upper right) from α7 of the monomer, and a large rotation of α9 to form the helical T (green). Heme pyrrole ring A propionate extends from its bent orientation in the monomer (purple, center, front) to interact with the pterin (white, right) in the dimer. The pterin interacts with the NH_2-terminal hook (rose), the NH_2-terminal pterin-binding segment (yellow), and the helical lariat (cyan).

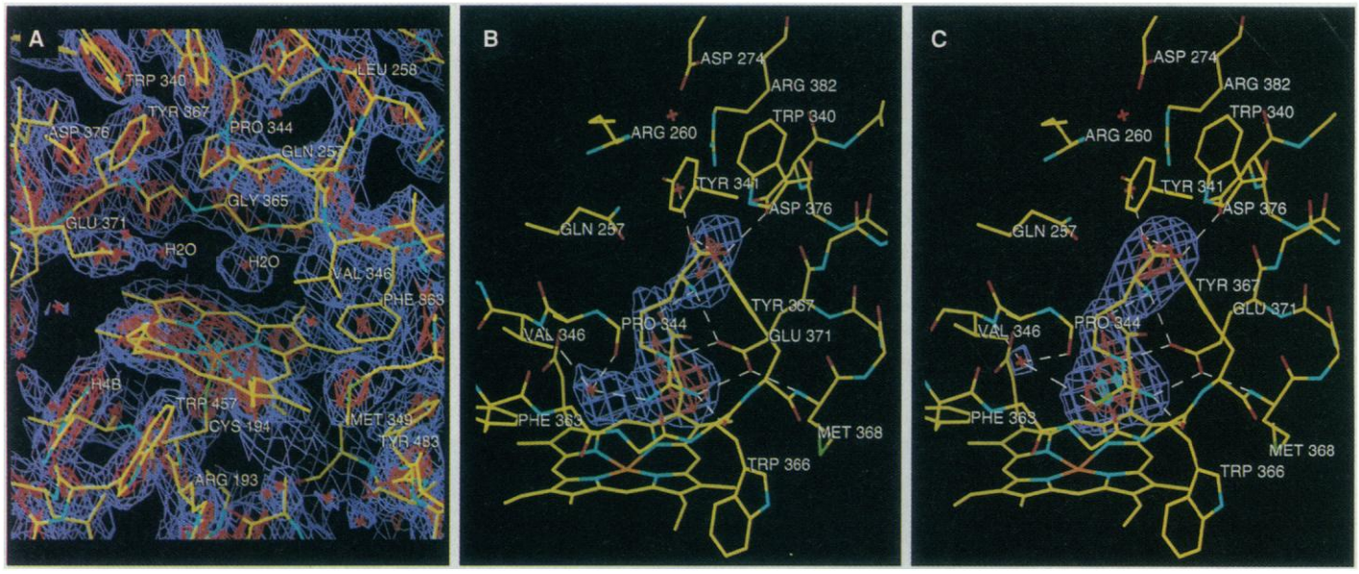

Fig. 4. Ligand-binding in the active center. (**A**) The H_4B-bound $iNOS_{ox}$ dimer (yellow carbons, red oxygens, and blue nitrogens) with active-center water molecules (red crosses), but without substrates or inhibitors [H_4B-H_2O (*8*)], viewed down the active channel and shown with its σA-weighted $2F_{obs} - F_{calc}$ electron density map (contours: purple 1.4σ, red 4.0σ, cyan 10σ). (**B**) L-Arg in the substrate binding site [H_4B-ARG (*7*, *8*)] from a view rotated roughly 180° about a vertical axis compared to (A). The σ_A-weighted $F_{obs} - F_{calc}$ omit electron density map (contours: purple 3.0σ, red 5.5σ), calculated with L-Arg and active-center waters removed from F_{calc}, depicts electron density for L-Arg and its associated water molecule (red crosses, left) in the absence of the minority contribution of the water-bound structure [see (A)] also present in H_4B-ARG (*8*). (**C**) SCit in the substrate-binding site [H_4B-SCIT (*7*, *8*)] viewed as in (B). The sulfur of the SCit thiourea group (green) is directed over the heme iron and highlighted by the highest contour level (cyan) in the σA-weighted $F_{obs} - F_{calc}$ SCit omit map (contours: purple 3.5σ, red 8σ, cyan 10σ). The omit electron density maps of (B) and (C) were averaged over noncrystallographic symmetry.

substrate binding, consistent with the inability of $iNOS_{ox}$ Δ114 to bind L-Arg (*5*). Pterin-induced changes in the heme environment that include ordering of the active-center channel, increased sequestration of the proximal heme ligand Cys^{194}, and extension of the negative heme A propionate away from the distal heme pocket (Figs. 2C and 3B) may account for the 50-mV increase in heme redox potential (*18*) and low-to-high spin shift of the ferric heme iron (*14*, *15*) in the presence of H_4B. Furthermore, increased basicity of the proximal Cys^{194} thiolate from sequestration in a more hydrophobic environment (Fig. 4A) may promote oxygen activation as well as the pterin-induced 70-fold increase in autoxidation of the ferrous heme-dioxy complex (*19*). However, close H_4B analogs that promote stable dimerization, substrate interactions, and heme spin shifts yet do not support NO synthesis (*14*, *20*) suggest that the structural coupling between H_4B and the heme propionate has a key catalytic role.

Aromatic amino acid hydroxylases (AAHs) use H_4B as an electron-supplying cofactor, oxidizing it to 4a-hydroxy-H_4B during catalysis (*21*). The NOS helical lariat contains residues conserved by the AAHs (*22*) that map near the catalytically important nonheme iron in pterin-free structures of tyrosine and phenylalanine hydroxylases (*23*). However, NOSs conserve only one of the two iron-binding His residues of AAHs (His^{471}, which contacts the pterin from the symmetry-related subunit) and lack a similar iron site, suggesting the respective pterin-binding sites have adapted for different chemistry. The absence of pterin recycling during steady-state NO synthesis (*24*) and of redox activity in single-turnover experiments (*25*) is consistent with H_4B modulating oxy-heme reactivity from the heme edge opposite to the NOS_{red} interaction site without H_4B participating in bona fide electron transfer.

In the structure of dimeric $iNOS_{ox}$ with H_4B but without bound substrate or inhibitor [H_4B-H_2O (*8*)] the ferric heme iron is pentacoordinate, and two water molecules interact with each other above the heme's distal face: one hydrogen bonds to substrate-binding residue Glu^{371} (see below), whereas the other resides 4.2 Å above the heme iron (Fig. 4A). An H_4B-mediated change from water-bound hexacoordinate to pentacoordinate heme is consistent with a shift to a majority of high-spin hemes (*5*, *14*, *15*) and a 30-fold rate increase in NO binding to the ferric heme iron (*26*). H_4B-promoted dissociation of heme-bound water likely reflects cofactor-induced changes in the heme environment with dimerization and pterin-binding and formation of a more favorable water site above the heme by an

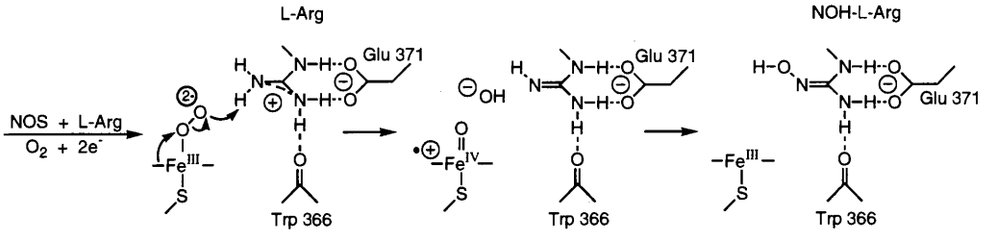

Fig. 5. Proposed L-Arg–assisted NOS oxygen activation. First, substrate L-Arg (only guanidinium shown) donates a proton to peroxo-iron, facilitating O–O bond cleavage and conversion to a proposed oxo-iron(IV) π-cation radical species, which then rapidly hydroxylates the neutral guanidinium to NOH-L-Arg, possibly through a radical-based mechanism (*3*).

extended Glu[371] conformation not seen in the NOS monomer.

The substrate L-Arg [H_4B-ARG (*7*, *8*)] and product analog SCit [H_4B-SCIT (*8*)] bind to the sequence-conserved active center in analogous conformations, suggesting that isozyme-specific inhibitors must interact with more variable, distal channel regions (Fig. 4). The L-Arg guanidinium and SCit thiourea groups both make two syn hydrogen bonds from their heme-distal and bridging nitrogens to both carboxylate oxygens of Glu[371], and one hydrogen bond from their heme-distal nitrogen to the carbonyl of Trp[366] at the otherwise hydrophobic bottom of the active-center channel (Fig. 4, B and C). The NOS porphyrin ring bends significantly to facilitate favorable stacking of the guanidinium or thiourea groups against pyrrole ring A. The Glu[371] residue is critical for substrate binding to NOS (*27*) and mediates inhibitor binding to $iNOS_{ox}$ Δ114 (*4*). Both the L-Arg and SCit carboxylate groups hydrogen bond to the Tyr[367] hydroxyl, a water molecule bridged to Arg[382], and the carboxylate of Asp[376], which may be protonated given its hydrogen-bonding partners and replacement by Asn in eNOS (Fig. 4). Interactions of the L-Arg α-amino and carboxylate groups with a network of hydrophilic side chains that are directly linked to structural elements involved in dimer formation (for example, the α7 helix), and to the same heme propionate that ligates H_4B (Fig. 3B), likely explain the cooperativity among dimerization, H_4B binding, and substrate binding (*2*, *14*, *15*, *28*).

Interactions of the L-Arg guanidinium and SCit thiourea groups at the bottom of the heme pocket (Fig. 4, B and C) suggest a mechanism for NO synthesis where proton donation from substrate L-Arg to bound dioxygen facilitates oxo-iron formation for the conversion of L-Arg to NOH–L-Arg, thereby neutralizing the L-Arg guanidinium group and discriminating between oxo- and peroxo-iron species in the two steps of NO synthesis (Fig. 5). It is likely that L-Arg binds when protonated, given the guanidinium interaction with Glu[371] and the heme π-electrons. The analogous conformations of substrate and product analog (Fig. 4, B and C) suggest that the bridging and heme-distal guanidinium nitrogens maintain their hydrogen bonds to Glu[371] and Trp[366] throughout catalysis. This leaves only the remaining terminal nitrogen well positioned (3.8 Å from the heme iron) and free to first donate a proton to peroxo-iron, facilitating oxygen-oxygen bond cleavage and reduction of the guanidinium charge, and to then react with the remaining electrophilic oxo-iron species to become hydroxylated (Fig. 5). Besides its proximity to the site of oxygen activation (Fig. 4B), L-Arg has a pK_a (K_a is the acid constant) at least 3 to 4 units less than water, the proposed proton donor to dioxy-iron in cytochrome P-450s (*3*). Further lowering of the L-Arg pK_a by distortion of its planar guanidinium is suggested by the electron density maps. Once L-Arg is converted to NOH–L-Arg, no proton is available to facilitate the breakdown of peroxo-iron, thereby allowing this dioxygen species to react with NOH–L-Arg to form citrulline and NO. Thus, the ligand-bound NOS structures suggest that NOS catalysis selects between two different reductive activations of dioxygen, depending on the protonation state of the substrate.

REFERENCES AND NOTES

1. S. Moncada and A. Higgs, *N. Engl. J. Med.* **329**, 2002 (1993); H. H. Schmidt and U. Walter, *Cell* **78**, 919 (1994); C. Nathan, *J. Clin. Invest.* **100**, 2417 (1997); K. S. Christopherson and D. S. Bredt, *ibid.*, p. 2424.
2. M. Marletta, *J. Biol. Chem.* **268**, 12231 (1993); O. W. Griffith and D. J. Stuehr, *Annu. Rev. Physiol.* **57**, 707 (1995); B. Mayer and E. R. Werner, *Nauyn-Schmiedeberg's Arch. Pharmacol.* **351**, 453 (1995); B. S. S. Masters *et al.*, *FASEB J.* **10**, 552 (1996); D. Stuehr, *Annu. Rev. Pharmacol. Toxicol.* **18**, 707 (1997).
3. M. Sono, M. P. Roach, E. D. Coulter, J. H. Dawson, *Chem. Rev.* **96**, 2841 (1996).
4. B. R. Crane *et al.*, *Science* **278**, 425 (1997).
5. D. K. Ghosh *et al.*, *Biochemistry* **36**, 10609 (1997).
6. Murine $iNOS_{ox}$ Δ65 (residues 66 to 498) with a fused COOH-terminal hexahistidine tag was overexpressed in *Escherichia coli* and purified in the absence of pterin as described (*5*). Hexagonal $iNOS_{ox}$ Δ65 crystals of space group $P6_122$ [cell dimensions 213.0 by 213.0 by 114.2 Å^3, two molecules per asymmetric unit, Matthews coefficient (V_M) = 4.0, solvent content = 70%] were grown overnight at 4°C by vapor diffusion from protein that had been complexed with freshly dissolved H_4B. Drops contained an equal-volume mixture of $iNOS_{ox}$ Δ65 (17 mg/ml) in 40 mM Hepps, pH 7.6, 10% glycerol, 1 mM dithiothreitol, 8 to 10 mM H_4B, with or without 10 mM L-Arg or SCit, and reservoir comprising 50 mM MES, pH 5.5 to 6.5, 5% w/v β-octyl-glucoside, and 18 to 21% Li_2SO_4 or $(NH_4)_2SO_4$.
7. An initial molecular replacement solution (correlation coefficient = 0.382 and R_{cryst} = 46.2%, for 10.0 to 4.5 Å resolution data) was found by AMoRe [L. Navaza, *Acta Crystallogr.* **D49**, 127 (1993)] in the hexagonal space group by using as probes two pruned structures (regions of high thermal parameters removed) of monomeric $iNOS_{ox}$ Δ114 (*4*) and 3.6 Å resolution diffraction data from an $iNOS_{ox}$ Δ65 crystal containing dihydrobiopterin (more stable than H_4B) collected on a rotating-anode x-ray source (overall $R_{sym} = \Sigma\Sigma_j |I_j - \langle I \rangle| / \Sigma\Sigma_j I_j$ = 18.7%, overall signal-to-noise ratio = $I/\sigma I$ = 15.4, 99% complete). (I_j is the intensity of observation j and $\langle I \rangle$ is the average of all observations.) Diffraction data were processed with DENZO [Z. Otwinowski and W. Minor, *Methods Enzymol.* **276**, 307 (1997)]. Crystallographic twofold symmetry generates two nonequivalent biological dimers in the $P6_122$ crystals from two $iNOS_{ox}$ subunits per asymmetric unit, which are themselves related by a noncrystallographic twofold axis, also perpendicular to the crystallographic 6_1 screw axis. Substantial changes in the dimeric interface regions of NOS were modeled with XFIT [D. E. McRee, *J. Mol. Graphics* **10**, 44 (1992)] to omit and symmetry-averaged $2F_{obs} - F_{calc}$, electron density maps calculated with DM [K. Cowtan, *Joint CCP4 ESF-EACBM Newsl. Protein Crystallog.* **31**, 34 (1994)] and pterin was built to the remaining difference density. We refined dimeric $iNOS_{ox}$ against the 3.6 Å resolution data first by rigid body and then by positional refinement and simulated annealing in X-PLOR [A. T. Brünger, J. Kuriyan, M. Karplus, *Science* **235**, 458 (1987)] to $R = \Sigma||F_{obs}| - |F_{calc}||/\Sigma|F_{obs}|$ = 27.5% and R_{free} = 32.7% (calculated against 5% of the reflections removed at random) using strict noncrystallographic symmetry (NCS) constraints and two grouped B factors per residue (F_{obs} and F_{calc} are the observed and calculated structure factors, respectively). The model resolution was extended to 2.6 Å by rebuilding to omit maps and positional refinement in X-PLOR against superior diffraction data collected on crystals containing H_4B and L-Arg (H_4B-ARG, overall R_{sym} = 5.7, $I/\sigma I$ = 22.0, 95.3% complete) at beamline X12C of the National Synchrotron Light Source (NSLS) with a Brandeis 1K charge-coupled device detector. R_{free} was optimized with mild NCS restraints placed on 71% of the protein backbone. The two independent $iNOS_{ox}$ dimers superimpose with a root-mean-square deviation (rmsd) of 0.4 Å on all Cα atoms and differ most at a non-equivalent lattice contact involving α1-α2. The $P6_122$ crystals diffracted anisotropically with greatest resolution-dependent intensity fall-off along the 6_1 screw axis (B11 = −0.79, B22 = −0.79, B33 = 43.38, B12 = 0.7, B13 = B23 = 0.0 from scaling F_{calc} to F_{obs} with an average model B factor of 25.0 Å^2). Application of an overall anisotropic scaling tensor to F_{obs} and intermittant recorrection for bulk solvent during X-PLOR refinement improved the final model (residues 77 to 100 and 108 to 496, 7208 scatterers, including 316 water molecules). R_{cryst} was 22.9% for all reflections (no σ cutoff) and R_{free} was 28.8% (the same free reflections chosen for all structures). Final model overall B factors (63.5 Å^2) matched those obtained by Wilson scaling (60.2 Å^2).
8. Crystals grown without ligand (H_4B-H_2O) or with thiocitrulline (H_4B-SCIT) gave diffraction data [collected at the Stanford Synchrotron Radiation Laboratory (SSRL) with a 34.5-cm Mar research image plate] that were isomorphous with H_4B-ARG (R_{sym} on merging <10%, cell dimensions <1% different). The H_4B-H_2O structure (7190 scatterers, 322 water molecules, R_{cryst} = 22.4%, R_{free} = 28.9%) and the H_4B-SCIT structure (7205 scatterers, 313 water molecules, R_{cryst} = 22.7%, R_{free} = 28.6%) were refined against 2.6 Å diffraction data (overall R_{sym} = 5.6%, $I/\sigma I$ = 28.2, 90.1% complete) and 2.7 Å diffraction data (overall R_{sym} = 5.7, $I/\sigma I$ = 18.2, 88.5% complete), respectively. All three final structures have excellent stereochemistry (rmsd from ideal bond lengths ≤0.008 Å and ideal bond angles ≤1.5°), with 99.2% of all residues in the most favored or otherwise allowed regions of ϕ/ψ space, as defined by PROCHECK [R. A. Laskowski *et al.*, *J. Appl. Crystallogr.* **26**, 283 (1993)]. No residues fall in disallowed regions. The H_4B-ARG structure was 0.55 occupied with L-Arg and its associated H_2O and 0.45 occupied with only H_2O (H_4B-H_2O) on the basis of systematic assessment of the residuals in $F_{obs} - F_{calc}$, electron density maps with varying ligand occupancies and extrapolated difference map calculations [U. K. Genick *et al.*, *Science* **275**, 1471 (1997)].
9. I. Rodriguez-Crespo, P. Moënne-Loccoz, T. M. Loehr, P. R. Ortiz de Montellano, *Biochemistry* **36**, 8530 (1997).
10. R. R. Cubberley *et al.*, *Biochem. J.* **323**, 141 (1997); B. S. S. Masters *et al.*, *Oxidants and Antioxidants in Biology World Congress Abstracts*, Santa Barbara, CA, 5 to 8 February 1998, L. Packer, Ed. (Oxygen Club of California, Berkeley, CA, 1998).
11. M. Wang *et al.*, *Proc. Natl. Acad. Sci. U.S.A.* **94**, 8411 (1997); D. S. Bredt *et al.*, *Nature* **351**, 714 (1991).
12. G. Garcia-Cardena *et al.*, *J. Biol. Chem.* **272**, 25437 (1997); J. B. Michel, O. Feron, K. Sase, P. Prabhakar, T. Michel, *ibid.*, p. 25907.
13. K. J. Baek, B. A. Thiel, S. Lucas, D. J. Stuehr, *ibid.* **268**, 21120 (1993).
14. A. Presta *et al.*, *Biochemistry* **37**, 298 (1998).
15. A. C. Gorren *et al.*, *ibid.* **35**, 16735 (1996).
16. P. Klatt *et al.*, *J. Biol. Chem.* **269**, 13861 (1994).

17. R. M. Chabin *et al.*, *Biochemistry* **35**, 9567 (1996).
18. A. Presta, A. M. Weber-Main, M. T. Stankovich, D. J. Stuehr, *J. Am. Chem. Soc.*, in press.
19. H. M. Abu-Soud, R. Gachhui, F. M. Raushel, D. J. Stuehr, *J. Biol. Chem.* **272**, 17349 (1997).
20. S. Pfeiffer *et al.*, *Biochem. J.* **328**, 349 (1997).
21. S. Kaufman, *Adv. Enzymol.* **67**, 77 (1993); T. Dix and S. J. Benkovic, *Acc. Chem. Res.* **21**, 101 (1988).
22. H. J. Cho, E. Martin, Q. Xie, S. Sassa, C. Nathan, *Proc. Natl. Acad. Sci. U.S.A.* **92**, 11514 (1995).
23. K. E. Goodwill *et al.*, *Nature Struct. Biol.* **4**, 578 (1997); H. Erlandsen *et al.*, *ibid.*, p. 995.
24. J. Giovanelli, K. L. Campos, S. Kaufman, *Proc. Natl. Acad. Sci. U.S.A.* **88**, 7091 (1991); K. E. Whiteveen, C. Giovanelli, S. Kaufman, *J. Biol. Chem.* **271**, 4143 (1996).
25. H. M. Abu-Soud, A. Presta, B. Mayer, D. J. Stuehr, *Biochemistry* **36**, 10811 (1997).
26. H. M. Abu-Soud, C. Wu, D. K. Ghosh, D. J. Stuehr, *ibid.*, in press.
27. R. Gachhui *et al.*, *ibid.* **36**, 5097 (1997); P. F. Chen *et al.*, *J. Biol. Chem.* **272**, 6114 (1997).
28. N. Sennequier and D. J. Stuehr, *Biochemistry* **35**, 5883 (1996).
29. Molecular surfaces were calculated with MS [M. L. Connolly, *Science* **221**, 709 (1983)] with a 1.4 Å probe. Figures were rendered in AVS [C. Upson *et al.*, *IEEE Comp. G.* **9**, 30 (1989)] and XFIT.

30. We thank C. D. Putnam, A. M. Bilwes, J. Skinner, and R. M. Sweet for help with data collection, NSLS and SSRL for use of data collection facilities, and J. R. Winkler and H. B. Gray for access to Beckman Institute resources. We also thank C. Mol, T. Macke, A. M. Bilwes, C. D. Putnam, M. Marletta, and B. S. S. Masters for helpful discussions. Supported by NIH grant HL58883 and a Helen Hay Whitney Fellowship to B.R.C. D.J.S. is an Established Investigator of the American Heart Association. The Protein Data Base codes are 1nod for H_4B-ARG, 2nod for H_4B-H_2O, and 3nod for H_4B-SCIT.

16 December 1997; accepted 11 February 1998

Species Distributions, Land Values, and Efficient Conservation

Amy Ando, Jeffrey Camm, Stephen Polasky, Andrew Solow*

Efforts at species conservation in the United States have tended to be opportunistic and uncoordinated. Recently, however, ecologists and economists have begun to develop more systematic approaches. Here, the problem of efficiently allocating scarce conservation resources in the selection of sites for biological reserves is addressed. With the use of county-level data on land prices and the incidence of endangered species, it is shown that accounting for heterogeneity in land prices results in a substantial increase in efficiency in terms of either the cost of achieving a fixed coverage of species or the coverage attained from a fixed budget.

The establishment of biological reserves in which development activity is prohibited or otherwise regulated is a common tool for species conservation. By making use of county-level data on the distribution of endangered species within the United States, Dobson *et al.* showed that a large number of endangered species are contained within a relatively small number of counties and concluded that "[i]f conservation efforts and funds can be expanded in a few key areas, it should be possible to conserve endangered species with great efficiency" (*1*, p. 553). This implicit equation of efficiency with the number of counties needed to achieve a given coverage of endangered species is reasonable when land prices are homogeneous. However, a better definition of efficiency takes account of differences in land prices between counties. Counties targeted in (*1*) included some of the highest priced land in the United States. Land purchases within these counties could quickly exhaust limited resources and lead to a lower total coverage than if the same resources were expended elsewhere. Even if land is protected by conservation easements or other regulations, rather than by outright purchase, protecting land in these counties may come at high opportunity costs.

Here, we study the effect of heterogeneous land prices on the efficient selection of reserve sites. We considered two versions of the reserve site selection problem (*2*). Under the first version, known as the set coverage problem (SCP), the objective is to minimize a loss function such as the number or cost of reserve sites subject to the constraint that all species are covered. Under the second version, called the maximal coverage problem (MCP), the objective is to maximize coverage subject to the constraint that the loss not exceed a specified amount.

Both the SCP and the MCP are examples of integer programming problems (*3*). Effective methods for solving them have been developed, and off-the-shelf optimization software has progressed to the point where it can be used effectively on large versions of the SCP and MCP (*4*). These methods have been applied to reserve site selection (*5*), and we applied them here.

We used county-level data on the estimated distribution of endangered species compiled by the U.S. Environmental Protection Agency Office of Pesticide Programs (*6*). These data, which are essentially the same as those used in (*1*), record by county the occurrence of all plants and animals protected or proposed for protection under the Endangered Species Act, as of 1995. The data cover a total of 911 species, subspecies, and populations and 2851 counties.

The corresponding county-level data on 1992 agricultural land values, in dollars per acre, have been compiled by the U.S. Department of Agriculture (*7*). Although it would be preferable to have the value of undeveloped land, the value of agricultural land, which reflects land market conditions, is a reasonable proxy. Values are available for 2822 counties in the species distribution list. We estimated the 29 missing values, which occur mainly in counties with minimal agricultural land, using values from previous years, neighboring counties, or both.

The goal of the analysis presented here was to compare optimal site selection when the loss is measured by the number of sites with optimal site selection when the loss is measured by the cost of the sites. To make this comparison, we assumed that all species within a county were covered in a site of unit area. Because the size of the unit area serves only to scale cost, for convenience, we took it to be 1 acre. More importantly, this assumption implies that all species within a county can be covered in the same unit area. In reality, not all of the endangered species within a county co-occur in the same site, and different species require reserves of different size for survival. In practice, the design of reserve sites, which is the subject of a large

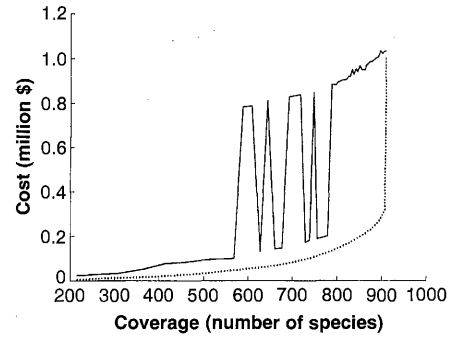

Fig. 1. Cost versus coverage for site-minimizing (solid curve) and cost-minimizing (dotted curve) solutions.

A. Ando, Resources for the Future, 1616 P Street, NW, Washington, DC 20036, USA.
J. Camm, Department of Quantitative Analysis and Operations Management, University of Cincinnati, Cincinnati, OH 45221, USA.
S. Polasky, Department of Agricultural and Resource Economics, Oregon State University, Corvallis, OR 97331, USA.
A. Solow, Woods Hole Oceanographic Institution, Woods Hole, MA 02543, USA.

*To whom correspondence should be addressed. E-mail: asolow@whoi.edu